ARTIFICIAL NOISE IN PIC CODES AND CONSEQUENCES ON LONG TERM TRACKING

Kazuhito Ohmi, KEK

Abstract

Emittance growth and beam loss due to nonlinear space charge force has been studies using Particle In Cell simulation. Artificial noise due to macro-particle statistics sometimes presents unphysical emittance growth. Artificial noise in Particle In Cell method disturbs the accurate prediction of the emittance growth. Using a fixed periodic space charge potential is one way to study emittance growth in a first step. Frozen potential and induced resonance are discussed in this paper. While emittance growth in a presence of real noise is serious issue in accelerators. Emittance growth under tune fluctuation is discussed with relation to studies in beam-beam effects.

INTRODUCTION

In Particle In Cell codes, space charge force is given by solving Poisson equation for macro-particles distribution mapped on grid space. Statistics of macro-particles, which cause a density modulation in the grid space, result in turn by turn fluctuation of the space charge force. Emittance conservation/growth in a periodic system is subject of our concern for the space charge effects. Artificial emittance growth caused by the fluctuation disturbs an accurate prediction, especially in long term simulation. Emittance growth in a fixed periodic potential can be discussed. In J-PARC, limitation of particle loss is very severe (1kW for the beam energy 1MW). Space charge potential is nearly determined by the core distribution. We can study emittance growth in the potential given by distribution which is initial or is fixed(frozen) at a time. Resonance and chaotic behavior in the fixed potential are subjects to be studied. It is important to study emittance growth dynamically changing potential for the next step.

Figure 1 shows evolution of x and σ_x in PIC simulation (SCTR) [1]. The space charge force is calculated turn-by-turn, where the number of macro-particle is 200,000. Fluctuations in x and σ_x are seen. The noises level is $\langle x \rangle \approx \pm 0.05$ mm ($0.5\%\sigma_{x,0}$) and $\sigma_x \approx 8.5 \pm 0.02$ mm ($0.2\%\sigma_{x,0}$). Higher order moments of the beam distribution must have similar fluctuation. Each particle experiences nonlinear force with the fluctuations in the simulation. Unphysical phenomena is seen in the simulation.

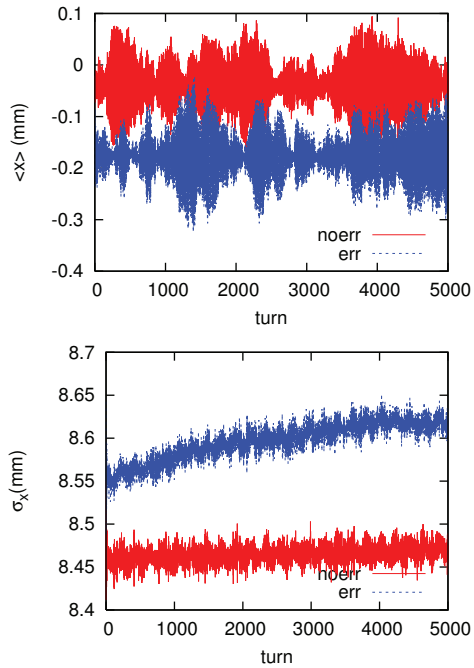

Figure 1: Evolution of x and σ_x in Particle-In-Cell simulation (SCTR). Red and blue lines are given for lattice without and with magnet alignment errors.

EXPERIENCES OF BEAM-BEAM INTERACTIONS IN COLLIDERS AND APPLICATION TO SPACE CHARGE EFFECTS

Experiences of Beam-beam Interactions in Colliders

Statistical noise in simulations is artifact, but noise in accelerator is sometimes real issue. Noise of collision offset from bunch-by-bunch feedback system degraded luminosity performance in KEKB [2]. Crab cavity is planned to be used in High Luminosity LHC. Noise in crab cavity phase and in bunch-by-bunch feedback system, which causes collision offset, has been studied in LHC [1, 3]. Theory for the noise effects was developed by G. Stupakov [4] and T. Sen et al.[5].

Potential (effective Hamiltonian) of the beam-beam interaction is expressed by

$$U(x) = \frac{N_p r_p}{\gamma_p} \int_0^\infty \frac{1 - e^{-x^2/(2\sigma_r^2+q)}}{2\sigma_r^2 + q} dq \delta_P(s) \quad (1)$$

ISBN 978-3-95450-173-1

where r_p and γ_p are the classical radius of the proton and the relativistic factor of the beam, respectively. The potential acts once per revolution at the collision point due to the periodic delta function $\delta_P(s)$ for the circumference. The potential is expanded by Fourier series as follows,

$$U(J,\psi) = \frac{N_p r_P}{\gamma_p} \sum_{k=0}^{\infty} U_k(a) \cos 2k\psi \delta_P(s) \qquad (2)$$

The potential with an offset Δx is given by

$$U(x+\Delta x) = U(x) + U'(x)\Delta x. \qquad (3)$$

Δx is a random variable fluctuated turn-by-turn. Change of J per collision is given for the potential by

$$\Delta J = -\frac{\partial U(x+\Delta x)}{\partial \psi} = -\frac{\partial U'}{\partial \psi}\Delta x. \qquad (4)$$

$\partial U(x)/\partial\psi$, which gives modulation of betatron motion, does not contribute emittance growth. Averaging the offset noise, diffusion of J per collision is given by

$$\langle \Delta J^2 \rangle = \frac{\partial U'}{\partial \psi}\frac{\partial U'}{\partial \psi}\langle \Delta x^2 \rangle \qquad (5)$$

The Fourier expansion of the potential with respect to the offset now becomes

$$U'(J,\psi) = \frac{N_p r_p}{2\gamma\sigma_r} \sum_{k=0}^{\infty} G_k(a) \cos(2k+1)\psi, \qquad (6)$$

where

$$G_k(a) = \sqrt{a}\left[U'_{k+1} + U'_k\right] + \frac{1}{\sqrt{a}}\left[(k+1)U_{k+1} - kU_k\right], \qquad (7)$$

and U'_k is the derivative evaluated at $a = J/(2\varepsilon)$. Diffusion of betatron amplitude is expressed by

$$\begin{aligned}\langle \Delta J^2 \rangle &\approx \frac{N_p^2 r_p^2 \Delta x^2}{8\gamma^2\sigma_r^2} \\ &\sum_{n=-\infty}^{\infty}\sum_{k=0}^{\infty}(2k+1)^2 G_k^2 \cos[(2k+1)n\mu] e^{-|n|/\tau} \\ &\approx \frac{N_p^2 r_p^2 \Delta x^2}{8\gamma^2\sigma_r^2}\sum_{k=0}^{\infty}\frac{(2k+1)^2 G_k(a)^2 \sinh 1/\tau}{\cosh 1/\tau - \cos(2k+1)\mu}. \end{aligned} \qquad (8)$$

The diffusion of betatron amplitude approximately linearly depends on its amplitude. The slope is expressed by

$$\frac{\langle \Delta J^2 \rangle}{a} = \frac{N_p^2 r_p^2}{8\gamma^2}\frac{\Delta x^2}{\sigma_r^2} \times 4.4. \qquad (9)$$

Convolution of the Eq.(9) by distribution function gives emittance growth rate and luminosity degradation as

$$\frac{\Delta L}{L} = \frac{\Delta\varepsilon}{\varepsilon} = \left(\xi\frac{\Delta x}{\sigma_r}\right)^2 \times 21.7. \qquad (10)$$

Weak-strong simulation, using frozen Gaussian colliding beam, has been done to study the effects of noise. [1] Figure 2 shows the luminosity degradation rate as function of offset noise amplitude. The rate given by formula Eq.(10) is plotted by three lines for the beam-beam tune shift values. The degradation rates agree well.

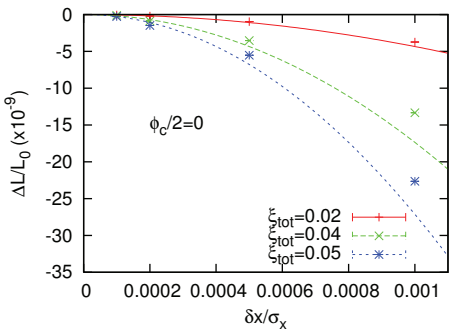

Figure 2: Diffusion rate without a crossing angle given by weak-strong simulation compared with predictions from Eq. (10).

Strong-strong simulation, in which Poisson solver is executed turn-by-turn using the particle in cell algorithm, has also been performed. Figure 3 shows the luminosity degradation rate. The agreement with formula Eq.(10) is again very well.

Application to Space Charge Force

The theory is applicable for space charge force. We sketch the theory. Beam distribution is assumed to be Gaussian in x-y space.

$$N\rho(x,y,z) = \frac{\lambda(z)}{2\pi\sigma_x\sigma_y}\exp\left(-\frac{x^2}{2\sigma_x^2} - \frac{y^2}{2\sigma_y^2}\right) \qquad (11)$$

where dispersion is taken into account in σ_x, $\sigma_x^2 = \beta_x\varepsilon_x + \eta_x^2(\Delta/p)^2$. Space charge force distributes along whole ring. The effective potential/Hamiltonian for one turn map is evaluated by integration of the space charge potential. Effective one turn potential (U) is given by

$$\begin{aligned}\prod_{i=0}\exp(-H_{i+1,i})\exp(-U_i) &= \exp(-H)\times \\ \prod\exp(H_{i+1,0})\exp(-U_i)&\exp(-H_{i+1,0}) \\ &= \exp(-H)\exp(-U) \end{aligned} \qquad (12)$$

Leading order expression of U is given by integration of U_i with taking into account of the betatron phase,

$$U = \int ds' U(s') = \frac{\lambda_p r_p}{\beta^2\gamma^3}\oint ds' \qquad (13)$$
$$\int_0^{\infty}\frac{1-\exp\left(-\frac{\beta_x(s')X(s,x')}{2\sigma_x^2+u} - \frac{\beta_y(s')Y(s,s')}{2\sigma_y^2+u}\right)}{\sqrt{2\sigma_x^2+u}\sqrt{2\sigma_x^2+u}}du$$

[1] Simulation using frozen potential is called weak-strong simulation, and turn-by-turn simulation is called strong-strong simulation in the beam-beam society.

ISBN 978-3-95450-173-1

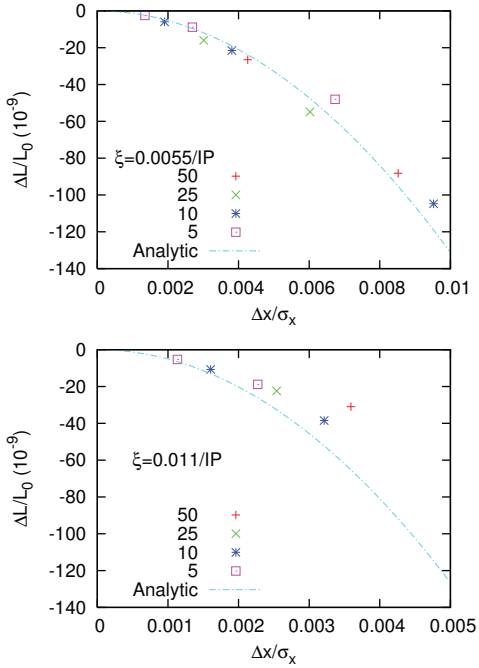

Figure 3: Diffusion rate given by strong-strong simulation compared with predictions from Eq. (10). Top and bottom are for the beam-beam tune shift 0.0055/IP and 0.011/IP, respectively.

where

$$\begin{aligned} X(s,s') &= \sqrt{2J_x}\cos(\varphi_x(s')+\phi_x(s)) \\ Y(s,s') &= \sqrt{2J_y}\cos(\varphi_y(s')+\phi_y(s)) \end{aligned} \quad (14)$$

Cross terms between space charge nonlinearities and between them of space charge and nonlinear magnetic components are neglected.

The Fourier component, which correspond to resonance strength, is given by

$$U_m(J_x,J_y) = \frac{\lambda_p r_p}{\beta^2\gamma^3}\oint ds \int_0^\infty \frac{du}{\sqrt{2\sigma_x^2+u}\sqrt{2\sigma_x^2+u}} \left[\delta_{m_x0}\delta_{m_y0} - \exp(w_x-w_y)(-1)^{(m_x+x_y)/2} I_{m_x/2}(w_x)I_{m_y/2}(w_y)e^{-im_x\varphi_x - im_y\varphi_y}\right]. \quad (15)$$

where H and U are one turn effective Hamiltonian of lattice transformation and space charge force, respectively.

The diffusion rate due to offset noise for the space charge potential Eqs.(13) and (23) is estimated by Eq.(8). Figure 4 shows the Fourier component/resonance strength for horizontal betatron phase as function of betatron amplitude. It is seen that lower component U_{40} is dominant. Diffusion rate due to the noise is evaluated by Eqs.(6) and (7) using U_k and U_k' evaluated by Fig.4.

Tune Fluctuation due to Ripple in J-PARC MR

We discuss effects of realistic noise in space charge dominant machine, J-PARC Main Ring. Tune modulation

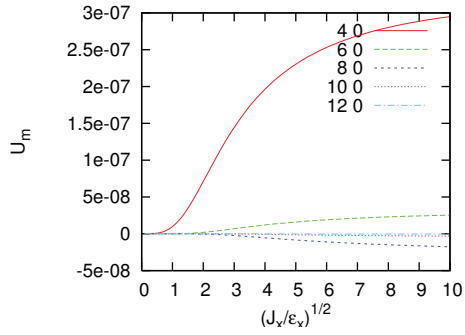

Figure 4: Resonance strength given by Eq.(23).

due to ripple of power supply has been observed around $\delta\nu \approx \pm 0.01$ with 50Hz in J-PARC MR,. Diffusion of J for tune modulation is evaluated by similar formula as the offset noise as follows,

$$\langle \Delta J^2\rangle \equiv \frac{\langle (J(N)-J(0))^2\rangle}{N} \quad (16)$$

$$= \frac{1}{N}\sum_{i=0}^{N}\sum_{j=0}^{N}\frac{\partial U_i}{\partial\psi}\frac{\partial U_j}{\partial\psi}\langle \Delta\psi_i\Delta\psi_j\rangle. \quad (17)$$

One summation is replaced by N, then another is expressed by summation of correlation of the noise.

$$\langle \Delta J^2\rangle = \sum_{n=-\infty}^{\infty}\frac{\partial U_\ell}{\partial\psi}\frac{\partial U_{\ell+n}}{\partial\psi}\langle \Delta\psi_\ell\Delta\psi_{\ell+n}\rangle. \quad (18)$$

The correlation is expressed by

$$\langle \Delta\psi_\ell\Delta\psi_{\ell+n}\rangle = 4\pi^2\Delta\nu^2 e^{-|n|/\tau_c} \quad (19)$$

where the correlation time is 50Hz, $\tau_c = 4,000$ turns (C=1567m). The diffusion rate of the betatron amplitude is expressed by,

$$\langle \Delta J^2\rangle = 8\pi^2\Delta\nu^2\sum_{k=0}^{\infty}k^2U_k^2\frac{\sinh 1/\tau_c}{\cosh 1/\tau_c - \cos 4\pi k\nu} \quad (20)$$

The diffusion rate is evaluated by $U_m \sim 10^{-7}$ m at $J \sim 4\varepsilon$ in Fig. 4.

$$\sqrt{\langle \Delta J^2\rangle} \sim 5.6\times10^{-10}\text{m at } J \sim 4\varepsilon = 40\times10^{-6}\text{m} \quad (21)$$

The beam loss is evaluated by convolution of the beam distribution and diffusion rate as function of J.

The magnet ripple should cause fluctuations not only tune but also beta function and dispersion; that is beam size fluctuate turn-by-turn. In this approach, treatment of resonance is not sufficient. Synchrotron motion may be also important. These effects are discussed in the future.

FROZEN MODEL IN SCTR CODE

SCTR code has developed to study space charge effects in J-PARC. The code is based on the ordinary Poisson

ISBN 978-3-95450-173-1

solver using particle in cell algorithm. Basically potential for space charge force is calculated every 1-2 meter ($< \beta_{xy}$) interval. The potential can be frozen and recalculated any time. The potential, which is represented by spline functions, is stored every points with 1-2 m interval.

Figure 5 shows dipole motion and beam size evolution in frozen mode (green) compared with those of non-frozen mode (blue). Dipole motion seen in non frozen mode is larger than that in frozen mode. It is difficult to say whether the motion in nonfrozen motion artifact, it enhances emittance growth in the simulation. Beam size in non-frozen model increase faster, but the difference is not remarkable. No quadrupole oscillation in non-frozen model is seen.

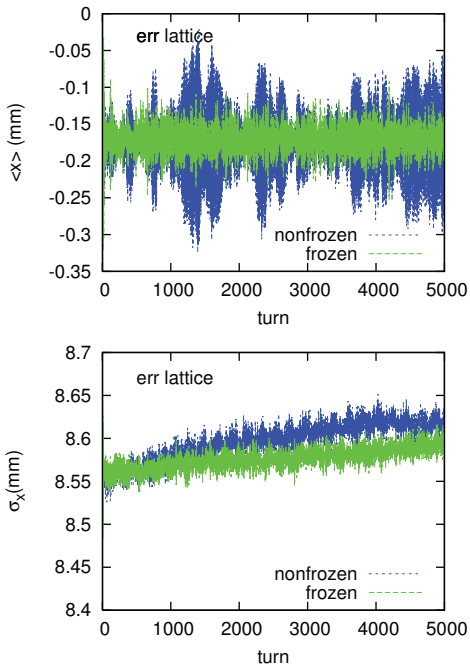

Figure 5: Dipole motion and beam size evolution in frozen mode. Green and blue lines are given by frozen and non-frozen modes, respectively.

Remarkable difference is seen in hallo distribution and beam loss. Comparison of frozen/non-frozen model was performed and presented at PAC07 [1], for example. Figure 6 shows the difference of frozen/non-frozen simulation. Red and magenta lines depict beam-loss for frozen model with 128×128 grid, 160k macro-particles and 64×64 grid, 40k macro-particles, respectively. The beam loss is independent of grid size/number and macro-particle number. Green and blue lines depict beam-loss for non-frozen model with 128×128 and 64×64 grid for 160k macro-particles, respectively. Cyan line depicts beam loss 64×64 grid for 40k macro-particles. Beam statistics strongly affect the beam loss in non-frozen model. This beam loss is artifact and should be more remarkable for high tune shift as is also seen in the beam-beam studies.

The frozen model is merit for computation performance using many processors. For PIC simulation, grid information must communicate between processors. The communication is necessary only when potential is recalculated in frozen model. Thus parallel computation using > 1000 processors is performed without performance loss. Figure 7 shows beam distribution during fully acceleration of J-PARC RCS 0.4GeV to 3GeV (top) and MR 3GeV to 30 GeV (bottom) [6].

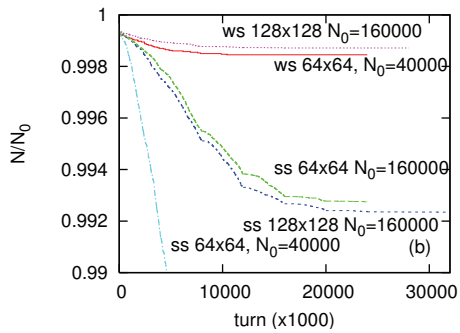

Figure 6: Evolution of beam loss in frozen and non-frozen model.

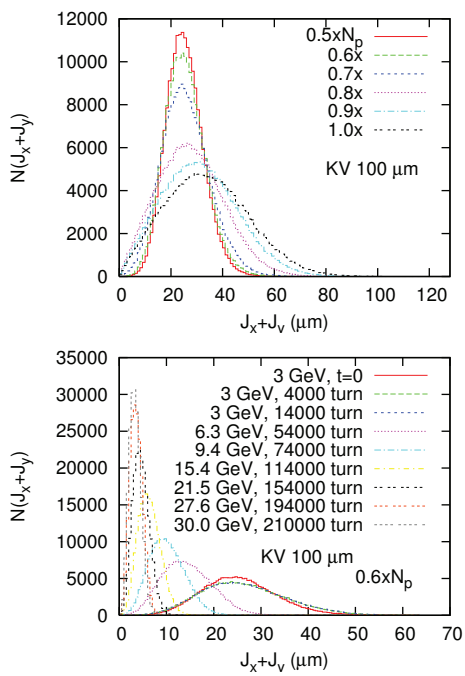

Figure 7: Evolution of the beam distribution during acceleration of J-PARC RCS(top) and MR(bottom).

Simulation for Choice of Operating Point in J-PARC MR

The frozen simulation is used for choice of operating point in J-PARC MR. MR has been operated at $(\nu_x, \nu_y) = (22.40, 20.75)$. Figure 8 shows beam loss map in the tune area, $22.0 < \nu_x < 22.5$ and $20.5 < \nu_y < 21.0$. Green area corresponds to the loss less than $\Delta N/N_0 < 10^{-4}$ in 5,000

ISBN 978-3-95450-173-1

turns. Wide green space is seen for the case without lattice errors in left picture. When errors are taken into account, sum x-y linear coupling resonance $\nu_x+\nu_y = 43$ clearly degrades beam loss. Dominant error is rotation of quadrupole magnets. Sum resonance component of x-y coupling is corrected, then the beam loss is recovered partially as shown in right picture.

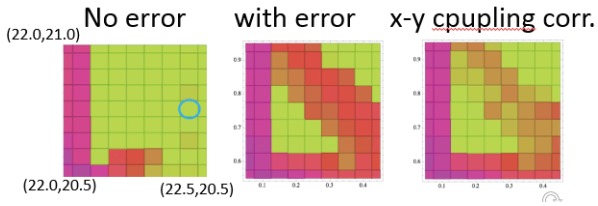

Figure 8: Beam loss map near present operating point. Loss of green mark is $\Delta N/N_0 < 10^{-4}$, in 5000 turns.

Beam loss map is obtained in wider area $20.0 < \nu_x < 23.0$ and $20.0 < \nu_y < 22.0$ as shown in Figure 9. Several good operating point are seen around $(\nu_x, \nu_y) = (21.38, 21.40)$ and (20.9,20.88). (22.38,22.40) is also good though it is out of the area. It is possible to study at injection energy in the area, but is hard for magnet strength at the top energy. Figure 10 shows the beam loss evolution at three operating points. Lattice error is taken into account in this simulation. At present operating point, coupling resonance is severe. but is somewhat recovered by correction using skew quadrupole magnets. For (21.38,21.40) and (22.38,22.40), degradation due to lattice error is not severe. The beam loss is far less than present point. Another motivation of choosing the operating point $\nu_x \approx \nu_y$ is better integrability due to angular momentum conservation in x-y motion [7, 8]. Beam test is being done for (21.38,21.40) and (22.38,22.40) in Nov 2014 [9].

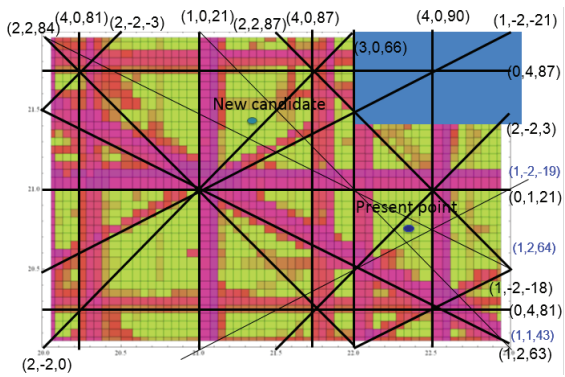

Figure 9: Beam loss map wide tune area, $20 < \nu_x < 23$, $20 < \nu_y < 22$. Lattice error is not taken into account; wiout and with coupling correction. Loss of green mark is $N/N_0 < 10^{-4}$ in 5,000 turns.

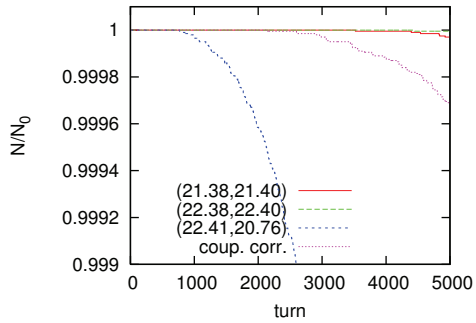

Figure 10: Beam loss at operating points (21.38,21.40), (22.38,22.40) and (22.40,20.75). Lattice error is taken into account.

EVALUATION OF RESONANCE WIDTH IN THE FROZEN POTENTIAL

In the frozen model, emittance growth is caused by chaotic diffusion near resonances. Resonances induced by the potential in the frozen model can be evaluated analytically, for example in Gaussian distribution.

Phase space structure near resonances are characterized by the resonance width. It is determined by their strength and tune slope for amplitude as follows,

$$\Delta J_x = 2\sqrt{\frac{U_{m_x,0}}{\Lambda}} \qquad \Lambda = \frac{\partial^2 U_{00}}{\partial J_x^2}. \tag{22}$$

The resonance width is estimated for Gaussian distribution by analytic method, The tune slope $\partial^2 U_{00}/\partial J_x^2$ is induced by space charge potential. That of space charge is dominant for that of nonlinear magnets as shown later. The tune slope is evaluated by $U_{00}(J_x, J_y)$ in Eq.(23).

$$U_{00}(J_x, J_y) = \frac{\lambda_p r_p}{\beta^2\gamma^3}\oint ds \int_0^\infty \frac{d\eta}{\sqrt{2+\eta}\sqrt{2r_{yx}+\eta}} (1 - e^{-w_x - w_y} I_0(w_x) I_0(w_y)). \tag{23}$$

where $r_{yx} = \sigma_y^2/\sigma_x^2$ and

$$w_x = \frac{\beta_x J_x/\sigma_x^2}{2+\eta}. \qquad w_y = \frac{\beta_y J_y/\sigma_y^2}{2+\eta/r_{yx}}. \tag{24}$$

$$\frac{\partial}{\partial J_x} = \frac{\beta_x/\sigma_x^2}{2+\eta}\frac{\partial}{\partial w_x}. \qquad \frac{\partial}{\partial J_y} = \frac{\beta_y/\sigma_x^2}{2r_{yx}+\eta}\frac{\partial}{\partial w_y}. \tag{25}$$

The tune shift is given by derivative of U_{00} for J_{xy} as follows,

$$2\pi\Delta\nu_x = -\frac{\partial U_{00}}{\partial J_x} = -\frac{\lambda_p r_p}{\beta^2\gamma^3}\oint ds \frac{\beta_x}{\sigma_x^2}\int_0^\infty \frac{e^{-w_x-w_y}d\eta}{(2+\eta)^{3/2}(2r_{yx}+\eta)^{1/2}} [(I_0(w_x) - I_1(w_x))I_0(w_y)], \tag{26}$$

ISBN 978-3-95450-173-1

$$2\pi\Delta\nu_y = -\frac{\partial U_{00}}{\partial J_y}$$
$$= -\frac{\lambda_p r_p}{\beta^2\gamma^3}\oint ds\frac{\beta_x}{\sigma_x^2}\int_0^\infty \frac{e^{-w_x-w_y}d\eta}{(2+\eta)^{1/2}(2r_{yx}+\eta)^{3/2}}$$
$$[I_0(w_x)(I_0(w_y)-I_1(w_y))]\,. \quad (27)$$

The tune slope is given by second derivative of U_0 as follows,

$$\frac{\partial^2 U_{00}}{\partial J_x^2} = -2\pi\frac{\partial\nu_x}{\partial J_x} \quad (28)$$
$$= \frac{\lambda_p r_p}{\beta^2\gamma^3}\oint ds\frac{\beta_x^2}{\sigma_x^4}\int_0^\infty \frac{e^{-w_x-w_y}d\eta}{(2+\eta)^{5/2}(2r_{yx}+\eta)^{1/2}}$$
$$\left[\left\{\frac{3}{2}I_0(w_x)-2I_1(w_x)+\frac{1}{2}I_2(w_x)\right\}I_0(w_y)\right],$$

$$\frac{\partial^2 U_{00}}{\partial J_x^2} = -2\pi\frac{\partial\nu_x}{\partial J_y} = 2\pi\frac{\partial\nu_y}{\partial J_x}$$
$$= \frac{\lambda_p r_p}{\beta^2\gamma^3}\oint ds\frac{\beta_x\beta_y}{\sigma_x^4}\int_0^\infty \frac{e^{-w_x-w_y}d\eta}{(2+\eta)^{3/2}(2r_{yx}+\eta)^{3/2}}$$
$$[(I_0(w_x)-I_1(w_x))(I_0(w_y)-I_1(w_y))]\,, \quad (29)$$

$$\frac{\partial^2 U_{00}}{\partial J_y^2} = -2\pi\frac{\partial\nu_y}{\partial J_y} \quad (30)$$
$$= \frac{\lambda_p r_p}{\beta^2\gamma^3}\oint ds\frac{\beta_y^2}{\sigma_x^4}\int_0^\infty \frac{e^{-w_x-w_y}d\eta}{(2+\eta)^{1/2}(2r_{yx}+\eta)^{5/2}}$$
$$\left[I_0(w_x)\left\{\frac{3}{2}I_0(w_y)-2I_1(w_y)+\frac{1}{2}I_2(w_y)\right\}\right],$$

where $I_0(x)' = I_1(x)$, $I_0(x)'' = (I_0(x)+I_2(x))/2$ are used.

Figure 11 shows tune spread $(\Delta\nu_{x,y}(J_x,J_y))$, slope $(\partial^2 U_0/\partial J_x^2)$, 4-th order resonance strength $(U_{4,0})$ and its width due to space charge force. The resonance width is visible size, 0.2ε, when $J_R=\varepsilon$.

Resonances and tune spread/slope are also induced by nonlinear magnets. One turn map is expanded by 12-th order polynomials. Taking at phase independent term, H_{00} is obtained as

$$\begin{aligned}H_{00}(\boldsymbol{J}) &= 3.43103\times10^{14}J_x^6+7.36914\times10^{14}J_x^5J_y+7.17029\times10^{11}J_x^5+2.34124\times10^{15}J_x^4J_y^2\\ &+ 1.70991\times10^{12}J_x^4J_y+1.43961\times10^{8}J_x^4+4.48931\times10^{15}J_x^3J_y^3+2.20917\times10^{12}J_x^3J_y^2\\ &+ 2.50211\times10^{8}J_x^3J_y+613899.J_x^3+3.33998\times10^{15}J_x^2J_y^4+1.79716\times10^{12}J_x^2J_y^3\\ &+ 7.07531\times10^{8}J_x^2J_y^2+809323.J_x^2J_y+1095.71J_x^2+7.58773\times10^{14}J_xJ_y^5\\ &+ 5.7438\times10^{11}J_xJ_y^4+4.55828\times10^{8}J_xJ_y^3+650655.J_xJ_y^2+2096.06J_xJ_y\\ &+ 4.11283\times10^{13}J_y^6+4.00294\times10^{10}J_y^5+5.3027\times10^{7}J_y^4+79924.4J_y^3+1106.98J_y^2\,.\end{aligned} \quad (31)$$

Figure 12 shows the tune shift and slope. Typical tune slope is $\partial^2 H_{00}/\partial x^2 = 1000 \sim 3000$. This value is similar for U_{00} at $J_x = 3^2\varepsilon$, namely tune slope of space charge is dominant for that of lattice nonlinearity at $J < 9\varepsilon(3\sigma)$, vice versa.

Resonance strength due to lattice nonlinearity is obtained by the one turn map. Table 1 shows the resonance

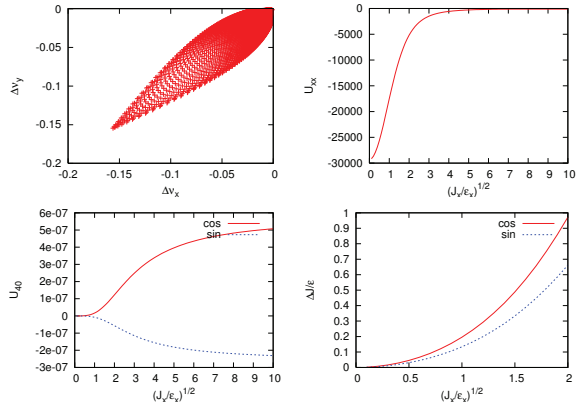

Figure 11: Tune spread $(\Delta\nu_{x,y}(J_x,J_y))$, slope $(\partial^2 U_0/\partial x^2)$, 4-th order resonance strength $(U_{4,0})$ and its width due to space charge force as function of J_R.

Table 1: Resonance width Under the Tune Slope Eq.(31)

mx	my	Jx	Jy	|G|	B0	B	BR
1	0	3.6E−05	0.0E+00		4.84E−08	1.88E−07	1.86E−07
2	0	3.6E−05	0.0E+00		2.47E−08	4.55E−08	4.66E−08
1	1	1.8E−05	1.8E−05		1.28E−25	1.67E−26	4.01E−09
0	2	0.0E+00	3.6E−05		5.55E−09	3.91E−09	2.69E−09
3	0	3.6E−05	0.0E+00		5.46E−08	1.29E−07	1.32E−07
2	1	1.8E−05	1.8E−05		2.09E−25	1.42E−26	1.42E−07
2	−1	1.8E−05	1.8E−05		2.16E−25	4.52E−27	7.96E−08
1	2	1.8E−05	1.8E−05		4.66E−08	1.78E−07	1.83E−07
1	−2	1.8E−05	1.8E−05		1.48E−07	2.72E−07	2.72E−07
0	3	0.0E+00	3.6E−05		1.42E−25	1.59E−26	1.10E−07
4	0	3.6E−05	0.0E+00		2.50E−07	2.51E−07	2.51E−07
3	1	1.8E−05	1.8E−05		1.93E−26	2.52E−27	6.80E−09
3	−1	1.8E−05	1.8E−05		1.61E−26	4.97E−27	7.04E−10
2	2	1.8E−05	1.8E−05		2.49E−08	5.90E−09	5.58E−09
2	−2	1.8E−05	1.8E−05		1.27E−08	8.40E−09	8.03E−09
1	3	1.8E−05	1.8E−05		2.52E−26	5.66E−27	3.56E−09
1	−3	1.8E−05	1.8E−05		1.63E−26	1.10E−26	8.42E−10
0	4	0.0E+00	3.6E−05		1.20E−08	1.45E−08	1.42E−08

width determined by resonance strength up to 4-th and the tune slope, Eq.(31). The width is reduced by space charge slope in Fig.11 depending on the resonant amplitude J_R.

In simulation with the frozen model, resonance width is seen in the phase space plot. Figure 13 shows the x phase space plot for parabolic (top) and Gaussian (bottom) beam, and compared with analitical estimate. Left and right plots is given for ideal and error lattices, respectively, at $(\nu_x,\nu_y) = (21..38, 21.40)$. 4-th order resonance is seen in parabolic, but not in Gaussian in ideal lattice. It is seen in Gaussian beam for error lattice. The 4-th order resonance is somewhat weaker than the previous estimation in Fig.11.

Figure 14 shows x phase space plot at $(\nu_x,\nu_y) = (22..41, 20.80)$. Top and bottom plots are for parabolic and Gaussian beam, respectively. Left and right are for ideal and error lattice, respectively. 3rd order resonance is seen. Separatrix structure of 3rd order resonance is destroyed in the error lattice. We guess this is due to x-y linear coupling

ISBN 978-3-95450-173-1

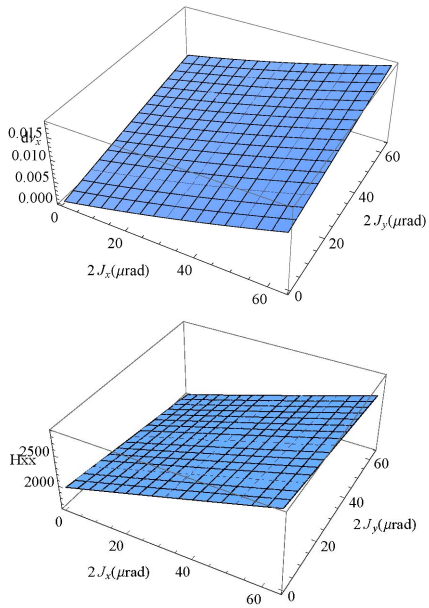

Figure 12: Tune spread, $\partial^2 H_{00}/\partial x^2$ induced by lattice nonlinearity.

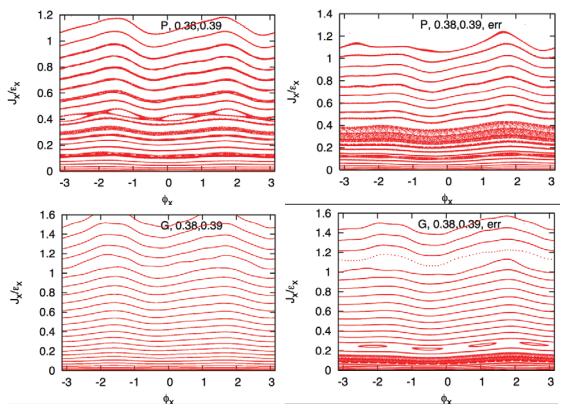

Figure 13: Phase space plot given by frozen model simulation for parabolic (top) and Gaussian (bottom) beam at $(\nu_x, \nu_y) = (21..38, 21.40)$. Left and right plots are for ideal and error lattices, respectively.

resonance $(\nu_x + \nu_y = 43)$. The two resonances excited simultaneously in this point.

TOY MODEL WITH THE TUNE SLOPE AND RESONANCE STRENGTH

We study a model with a given tune slope and resonance strength. This is an example of Hamiltonian,

$$H = \mu_0 J + \left(J + \frac{e^{-2aJ}}{2a} \right) + bJ \cos m\phi \qquad (32)$$

The tune shift is given by

$$\mu = \frac{\partial H}{\partial J} = \mu_0 + (1 - e^{-2aJ}). \qquad (33)$$

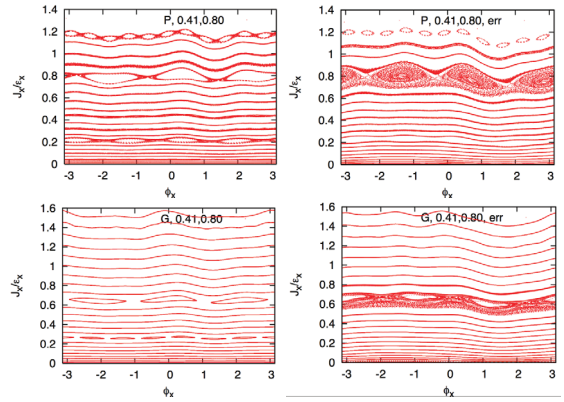

Figure 14: Phase space plot at $(\nu_x, \nu_y) = (22..41, 20.80)$. Top and bottom plots are for parabolic and Gaussian beam, respectively. Left and roght are for ideal and error lattice, respectively.

For small amplitude tune shift $2aJ$, where $a > 0$. The tune slope is given by

$$\frac{\partial^2 H}{\partial J^2} = 2ae^{-2aJ}. \qquad (34)$$

Half width of the resonance is expressed by

$$\Delta J = \sqrt{\frac{2bJ_R}{ae^{-2aJ_R}}}. \qquad (35)$$

Symplectic integration is performed by $H(J, \phi)$ as follows,

$$\begin{aligned} J_{n+1} &= \frac{J_n}{1 - bm \sin m\phi_n} \qquad (36) \\ \phi_{n+1} &= \phi_n + \mu + (e^{-2aJ_{n+1}} - 1) + b \cos m\phi_n \end{aligned}$$

where J_n and ϕ_n are those of n-th turn.

We study two cases of parameters,

- $a = 0.5, b = 0.002, m = 4, \mu = 2\pi \times 0.203$
- $a = 0.5, b = 0.0002, m = 4, \mu = 2\pi \times 0.203$

The resonance widths are given as (1) $\Delta J = 0.07$ and (2) =0.02. The betatron amplitude, where the resonance hits, is $J_R = 0.38$.

The model is tracked using the two sets of parameters. Figure 15 shows phase space trajectories. 4-the order resonance is seen, and their position (J_R) and widths agree with the formula, Eqs.(33) and (35)

Tune spread area modulates due to synchrotron oscillation. To study the effect, the strength of tune shift term a is made a modulation as

$$a = \frac{a_0}{2}(1 + \cos 2\pi\nu_s n). \qquad (37)$$

The resonant amplitude move to larger amplitude for small a. The model does not match to space charge force in this

ISBN 978-3-95450-173-1

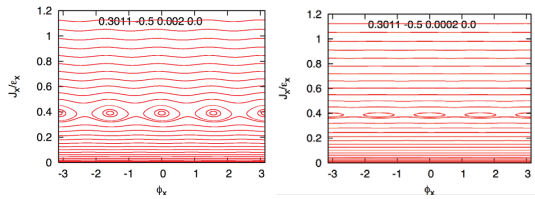

Figure 15: Phase space trajectory for the model map, Eq.(36). Left and right plots correspond to parameters (1) and (2), respectively.

point. This model should be improved in the future. Figure 16 shows phase space plot taking into account of the effective synchrotron motion. Chaotic area drastically increases due to the synchrotron motion. Figure 17 shows the emittance growth of the model with Eqs.(36) and (37). We can see the emittance growth depending on the resonance width.

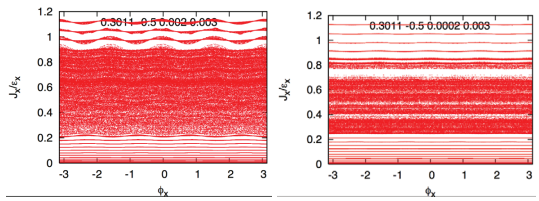

Figure 16: Phase space trajectory for the model map taking into account of effective synchrotron motion, Eqs.(36) and (37). Left and right plots correspond to parameters (1) and (2), respectively.

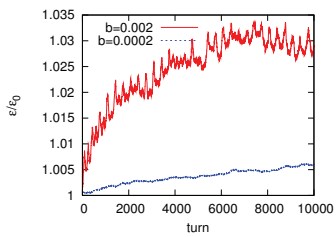

Figure 17: Emittance growth of the model with Eqs.(36) and (37).

SUMMARY

Noise of PIC simulation induces artificial emittance growth. While collision offset noise in colliders, which is similar situation in computer simulation, is real issue. Noise of power supply ripple in J-PARC can be treated similar way.

To avoid noise frozen model is used as cross check of ordinary non-frozen model simulation. The model is limited to study incoherent emittance growth. Tools to study the incoherent resonance effect is being prepared. Simple toy model was executed to understand resonance phenomena. Synchrotron motion is important for emittance growth combined with the resonances.

Complex accelerator system with complex space charge effects may be represented by simple several lines of Hamiltonian, though simple accelerator system with fundermental space charge effect is complex.

The author thanks fruitful discussions with Drs. H. Harada, S. Igarashi, A. Molodozhentsev and Y. Sato.

REFERENCES

[1] K. Ohmi et al., "Beam-beam effect with an external noise in LHC", PAC07.

[2] K. Ohmi, proceedings of PAC05, TPPP004.

[3] S. Paret, J. Qiang, Proceeding of Bbeam-beam 2013, CERN.

[4] G. Stupakov, SSCL-560 (1991).

[5] T. Sen and J.A. Ellison, Phys. Rev. Lett. 77, 1051 (1996).

[6] K. Ohmi et al., proceedings of HB2010, WEO1A04.

[7] V.V. Danilov, E.A. Perevedentsev, "An approach to integrability in round colliding beams," Proc. Advanced ICFA Beam Dynamics Workshop on Beam Dynamics Issues for e+e- Factories, Frascati, 321 (1997).

[8] K. Ohmi and K. Oide, Phys. Rev. ST-AB 10, 014401 (2007).

[9] Y. Sato et al., proceedings of HB2014.

ISBN 978-3-95450-173-1